Nonlinear seismic response for the 2011 Tohoku earthquake: borehole records versus 1Directional - 3Component propagation models

Maria Paola Santisi d'Avila, Jean-François Semblat

Nonlinear seismic response for the 2011 Tohoku earthquake: borehole records versus 1Directional - 3Component propagation models

Maria Paola Santisi d'Avila[1] and Jean-François Semblat[2]

[1] *Université de Nice-Sophia Antipolis, LJAD, 06108 Nice, France. Email: msantisi@unice.fr*

[2] *Université Paris Est, IFSTTAR/GERS/SV, 77447 Marne la Vallée, France.*

Accepted *date*. Received *date*; in original form *date*

Abbreviate title: **1D-3C seismic response during the Tohoku earthquake**

Corresponding author:

Maria Paola Santisi d'Avila

Laboratoire Jean Alexandre Dieudonné

University of Nice Sophia Antipolis

Address: 28, Avenue de Valrose - 06108 Nice - France

Phone: +33(0)4 92 07 62 33

Email: msantisi@unice.fr

SUMMARY

The seismic response of surficial multilayered soils to strong earthquakes is analyzed through a nonlinear one-directional three-component (1D-3C) wave propagation model. The three components (3C-polarization) of the incident wave are simultaneously propagated into a horizontal multilayered soil. A 3D nonlinear constitutive relation for dry soils under cyclic loading is implemented in a quadratic line finite element model. The soil rheology is modeled by mean of a multi-surface cyclic plasticity model of the Masing-Prandtl-Ishlinskii-Iwan type. Its major advantage is that the rheology is characterized by few nonlinear parameters commonly available. Previous studies showed that, when comparing one to three component unidirectional wave propagation simulations, the soil shear modulus decreases and the dissipation increases, for a given maximum strain amplitude. The 3D loading path due to the 3C-polarization leads to multiaxial stress interaction that reduces soil strength and increases nonlinear effects. Nonlinearity and coupling effects between components are more obvious with decreasing seismic velocity ratio in the soil and increasing vertical to horizontal component ratio for the incident wave. This research aims at comparing computed ground motions at the surface of soil profiles in the Tohoku area (Japan) with 3C seismic signals recorded during the 2011 Tohoku earthquake. The 3C recorded downhole motion is imposed as boundary condition at the base of soil layer stack. Notable amplification phenomena are shown, comparing seismograms at the bottom and at the surface. The 1D-3C approach evidences the influence of the 3D loading path and input wavefield polarization. 3C motion and 3D stress and strain evolution are evaluated all over the soil profile. The triaxial mechanical coupling is pointed out by observing the variation of the propagating wave polarization all along the duration of seismograms. The variation of the maximum horizontal component of motion with time, as well as the influence of the vertical component, confirm the interest of taking into account the 3C nonlinear coupling in 1D wave propagation models for such a large event.

KEYWORDS

Earthquake ground motions, Site effects, Wave propagation, Computational seismology.

1 INTRODUCTION

Surficial soil layers act as a filter on propagating seismic waves, changing the frequency content, duration and amplitude of motion. Amplification phenomena depend on path layering, velocity contrast and wave polarization (Bard & Bouchon 1985). Furthermore, seismic waves due to strong ground motions propagating in surficial soil layers may both reduce soil stiffness and increase nonlinear effects. The nonlinear behavior of the soil may have beneficial or detrimental effects on the dynamic response at the surface, depending on the energy dissipation process. The three-dimensional (3D) loading path influences the stresses into the soil and thus its seismic response.

This research aims at providing a model to study the local seismic response in case of strong earthquakes affecting alluvial sites. The proposed approach allows to assess possible amplifications of seismic motion at the surface, influenced by the geological and geotechnical structure. Such parameters as the three-component motion and 3D stress and strain states along the soil profiles may thus be computed in order to investigate in deeper details the effects of soil nonlinearity, seismic wave polarization and multiaxial coupling under 3C cyclic motion.

Past studies have been devoted to one-directional shear wave propagation in a multilayered soil profile (1D-propagation) considering one motion component only (1C-polarization). One-directional wave propagation analyses are an easy way to investigate local seismic hazard for strong ground motions. Several 1D propagation models were developed, to evaluate the 1C ground response of horizontally layered sites, reproducing soil behavior as equivalent linear (SHAKE, Schnabel *et al*. 1972; EERA, Bardet *et al*. 2000; Kausel & Assimaki, 2002), dry nonlinear (NERA, Bardet *et al*. 2001, X-NCQ, Delépine *et al*. 2009) and saturated nonlinear (DESRA-2, Lee & Finn 1978; TESS by Pyke 2000 from PEERC 2008; DEEPSOIL, Hashash and Park 2001; DMOD2, Matasovic 2006). The 1D-1C approach is a good approximation in the case of low strains within the linear range (superposition principle, Oppenheim *et al*. 1997). The effects of axial-shear stress interaction in multiaxial stress states have to be taken into account for higher strain levels, in the nonlinear range. The main difficulty is to find a constitutive model that reproduces faithfully the nonlinear and hysteretic behavior of soils under cyclic loadings, with the minimum number of parameters characterizing soil properties. Moreover, representing the 3D hysteretic behavior of soils, to reproduce the soil dynamic response to a three-component (3C) wave propagation, means considering three motion components that cannot be computed separately (SUMDES code, Li *et al*. 1992; SWAP_3C code, Santisi d'Avila *et al.* 2012, 2013). Li (1990) incorporated the 3D cyclic plasticity soil model proposed by Wang *et al*. (1990) in a 1D finite element procedure (Li *et al*. 1992), in terms of effective stress, to simulate the one-directional wave propagation accounting for pore pressure in the soil. However, this complex rheology needs a large number of parameters to characterize the soil model at field sites.

In this research, the specific 3D stress-strain problem for seismic wave propagation along one-direction only (1D-3C approach) is solved using a constitutive model of the Masing-Prandtl-Ishlinskii-Iwan (MPII) type (Iwan 1967, Joyner 1975, Joyner & Chen 1975), as called by Segalman & Starr (2008), depending only on commonly measured properties: mass density, shear and pressure wave velocities and the nonlinear shear modulus reduction versus shear strain curve. Due to its 3D nature, the procedure can handle both shear wave and compression wave simultaneously and predict the ground motion taking into account the wave polarization.

Most of previously mentioned one-directional one-component (1D-1C) time domain nonlinear approaches use lumped mass (DESRA-2, Lee & Finn 1978; DEEPSOIL, Hashash and Park 2001; DMOD2, Matasovic 2006) or finite difference models (TESS by Pyke 2000 from PEERC 2008). In this research, the MPII constitutive model is implemented in a finite element scheme, allowing the evaluation of seismic ground motion due to three-component strong earthquakes and proving the importance of a three-directional shaking modelling.

According to Santisi *et al*. (2012), the main difference between three superimposed one-component ground motions (1D-1C approach) and the proposed one-directional three-component propagation model (1D-3C approach) is observed in terms of ground motion time history, maximum stress and hysteretic behavior, with more nonlinearity and coupling effects between components. These consequences are more obvious with decreasing seismic velocity ratio (and Poisson's ratio) in the soil and increasing vertical to horizontal component ratio of the incident wave.

Santisi d'Avila *et al.* (2012, 2013) investigated the influence of soil properties, soil profile layering and 3C-quake features on the local seismic response of multilayered soil profiles, applying an absorbing boundary condition at the soil-bedrock interface (Joyner & Chen 1975), in the 1D-3C wave propagation model. The same elastic bedrock modelling was adopted by Lee & Finn (1978), Li (1990) and Bardet *et al*., (2000, 2001). Halved seismograms recorded at the top of close outcropping rock type profiles are applied as 3C incident wave in analyzed soil profiles. The accuracy of predicted soil motion depends significantly on the rock motion characteristics. This kind of procedure cannot be proposed for design, criteria for choosing associated rock motions not being known precisely (PEERC 2008).

In the present research, the goal is to appraise the reliability of the 1D-3C propagation model using borehole seismic records. In this case, the 3C signal contains incident and reflected waves, so an imposed motion at the base of the soil profile is more adapted as boundary condition. The validation of the proposed 1D-3C propagation model is undertaken comparing the three-component signals of the 11 March 2011 Mw 9 Tohoku earthquake, recorded at the surface of alluvial deposits in the Tohoku area (Japan), with the numerical time histories at the top of stacked horizontal soil layers. Seismic records with high vertical to horizontal acceleration ratio are applied in this research, to investigate the impact of such large ratios. Soil and quake properties are related to the same profile, increasing the accuracy of results and consequently allowing more quantitative analyses.

The proposed 1D-3C wave propagation model with a boundary condition in acceleration at depth is presented in Section 2. Soil properties and quake features for the analyzed cases are presented in Section 3. Anderson's criteria (Anderson 2004) are used to assess the reliability of the proposed model in Section 4, estimating the goodness of fit of synthetic signals compared with seismic records. In this section, hysteretic loops and component ration are also computed. The conclusions are developed in Section 5.

2 1D-3C PROPAGATION MODEL USING BOREHOLE RECORDS

The three components of seismic motion are propagated along one direction in nonlinear soil stratification. The multilayered soil is assumed infinitely extended along the horizontal directions. The wide extension of alluvial basins induces negligible surface wave effects

(Semblat & Pecker, 2009). Shear and pressure waves propagate vertically in the z-direction. These hypotheses yield no strain variation in the x- and y-direction. At a given depth, the soil is assumed to be a continuous, isotropic and homogeneous medium. Small and medium strain levels are considered during the process.

2.1 3D nonlinear hysteretic model

The adopted Masing-Prandtl-Ishlinskii-Iwan rheological model for soils (Bertotti & Mayergoyz 2006; Segalman & Starr 2008) is suggested by Iwan (1967) and applied by Joyner (1975) and Joyner & Chen (1975) in a finite difference formulation. It has been selected because it emulates a 3D behavior, nonlinear for both loading and unloading and, above all, because the only necessary parameter to characterize the soil hysteretic behavior is the shear modulus decay curve $G(\gamma)$ versus shear strain γ.

The soil nonlinearity reduces the shear modulus and increases the damping, for increasing strain levels, for one-component shaking, as evidenced by the shear modulus decay curve and damping ratio curve of the material, given by laboratory tests or inversion techniques (Assimaki *et al*., 2011). The nonlinear shear stress-strain curve (τ, γ) during a one-component monotonic loading is referred to as a backbone curve $\tau = G(\gamma)\gamma$, obtained knowing the shear modulus decay curve $G(\gamma)$. The backbone curve is assumed, in the present study, adequately described by a hyperbolic function (Hardin & Drnevich 1972) as

$$\tau(\gamma) = G(\gamma)\gamma = \left[G_0 \middle/ \left(1 + \left|\gamma/\gamma_r\right|\right) \right] \gamma \tag{1}$$

however, the MPII constitutive model does not depend on the applied shear modulus decay curve. It could also incorporate curves obtained from laboratory dynamic tests, as resonant column test (Semblat & Pecker, 2009), on soil samples. The reference shear strain γ_r corresponds to an actual tangent shear modulus equivalent to 50% of the initial shear modulus G_0. Nonlinear shear stress-strain curve is modelled using a series of mechanical elements, having different stiffness and increasing sliding resistance. Iwan (1967) modifies the 1D multi-linear plasticity mechanism $\tau_k = G_k\left(\gamma_k, \gamma_{k-1}, \tau_{k-1}\right)\gamma_k$, where $G_k = \left(\tau_k - \tau_{k-1}\right) / \left(\gamma_k - \gamma_{k-1}\right)$ at each step k, by introducing a yield surface in the stress space. The MPII model is a multi-surface elasto-plastic mechanism with hardening, that takes into account the nonlinear hysteretic behavior of soils in a three-dimensional stress state, based on the definition of a series of nested yield surfaces, according to von Mises' criterion. The stress level depends on the strain increment and strain history but not on the strain rate. Therefore, the energy dissipation process is purely hysteretic, without viscous damping.

The implementation of the MPII nonlinear cyclic constitutive model in the proposed finite element scheme is presented in detail by Santisi d'Avila *et al.* (2012).

The MPII hysteretic model is applied in the present research for dry soils in a three-dimensional stress state under cyclic loading, allowing a multiaxial total stress analysis. The material strength is lower under triaxial loading rather than for simple shear loading. From one to three components unidirectional propagating wave, the shear modulus decreases and the dissipation increases, for a given maximum strain amplitude.

Strains are in the range of stable nonlinearity, where, for one-component loading, both shear modulus and damping ratio do not depend on the number of cycles and the shape of hysteresis loops remains unvaried at each cycle. In the case of three-component loading, the shape of the hysteresis loops changes at each cycle for shear strains in the same range. According to Santisi *et al*. (2012), hysteresis loops for each horizontal direction are altered as a consequence of the interaction between loading components.

Large strain rates and liquefaction phenomena are not adequately reproduced without taking into account pore pressure effects. Constitutive behavior models for saturated soils should allow to reach larger strains with proper accuracy in future 1D-3C formulations (Viet Anh *et al*., 2013).

2.2 Spatial discretization

The stratified soil is discretized into a system of horizontal layers, parallel to the xy plane, by using a finite element scheme (Fig. 1), including quadratic line elements with three nodes. According to the finite element modeling, the discrete form of equilibrium equations, is expressed in the matrix form as

$$\mathbf{M}\,\ddot{\mathbf{D}} + \mathbf{F}_{\text{int}} = \mathbf{0} \tag{2}$$

where $\mathbf{M}$ is the mass matrix, $\ddot{\mathbf{D}}$ is the acceleration vector that is the second time derivative of the displacement vector $\mathbf{D}$. $\mathbf{F}_{\text{int}}$ is the vector of nodal internal forces. A non-zero load vector and damping matrix appear in Santisi d'Avila *et al.* (2012, 2013) where an absorbing boundary condition is assumed. In this research, there are no damping terms in the equilibrium problem, because the boundary condition is an imposed motion, downhole records being considered. Figure 1

The differential equilibrium problem (2) is solved according to compatibility conditions, the hypothesis of no strain variation in the horizontal directions, a three-dimensional nonlinear constitutive relation for cyclic loading and the boundary conditions described below. The Finite Element Method, as applied in the present research, is completely described in the works of Batoz & Dhatt (1990), Reddy (1993) and Cook *et al*. (2002).

Discretizing the soil column into n_e quadratic line elements and consequently into $n = 2\,n_e + 1$ nodes (Fig. 1), having three translational degrees of freedom each, yields a $3n$-dimensional displacement vector $\mathbf{D}$ composed by three blocks whose terms are the displacements of the n nodes in x-, y- and z-direction, respectively. Soil properties are assumed constant in each finite element and soil layer.

Mass matrix $\mathbf{M}$ and the vector of internal forces $\mathbf{F}_{\text{int}}$ are presented in the Appendix.

The assemblage of $(3n \times 3n)$-dimensional matrices and $3n$-dimensional vectors is independently done for each of the three $(n \times n)$-dimensional submatrices and n-dimensional subvectors, respectively, corresponding to x-, y- and z-direction of motion.

The distance between nodes in the three-node line finite element scheme is $H_j \big/ \left(2\, n_e^j\right)$, where n_e^j is the number of elements in the layer j having the thickness H_j (Fig. 1). It is assumed not higher than $d_{\max} = 1\,\text{m}$ ($< 1.5\,\text{m}$ for thick rock layers). The minimum number of nodes per wavelength r is such as $\lambda / r \le d_{\max}$. This implies that $r \ge \lambda / d_{\max}$. The seismic signal wavelength λ is equal to v_s / f, where f is the assumed maximum frequency of the input signal and v_s is the assumed minimum shear velocity in the medium.

2.3 Time discretization

The finite element model and the soil nonlinearity require spatial and time discretization, respectively, to permit the problem solution (Hughes 1987; Crisfield 1991). The rate type constitutive relation between stress and strain is linearized at each time step. Accordingly, equation (2) is expressed as

$$\mathbf{M}\,\Delta\ddot{\mathbf{D}}_k^i + \mathbf{K}_k^i\,\Delta\mathbf{D}_k^i = \mathbf{0} \tag{3}$$

where the subscript k indicates the time step t_k and i the iteration of the problem solving process, as explained below. The stiffness matrix $\mathbf{K}_k^i$ is presented in the Appendix.

The step-by-step process is solved by the Newmark's algorithm that is an implicit self-starting unconditionally stable approach for one-step time integration in dynamic problems (Newmark 1959; Hilber *et al*. 1977; Hughes 1987). According to Newmark's procedure, the displacement variation is expressed as follows:

$$\Delta \mathbf{D}_k^i = \Delta t\, \dot{\mathbf{D}}_{k-1} + \frac{\Delta t^2}{2} \ddot{\mathbf{D}}_{k-1} + \beta\, \Delta t^2\, \Delta \ddot{\mathbf{D}}_k^i \tag{4}$$

Equations (3) and (4) yield

$$\bar{\mathbf{M}}_k^i\, \Delta \ddot{\mathbf{D}}_k^i = \mathbf{A}_k^i \tag{5}$$

where the modified mass matrix is defined as

$$\bar{\mathbf{M}}_k^i = \mathbf{M} + \beta\, \Delta t^2\, \mathbf{K}_k^i \tag{6}$$

and $\mathbf{A}_k^i$ is a vector depending on the motion at the previous time step, given by

$$\mathbf{A}_k^i = -\left(\Delta t\, \mathbf{K}_k^i\right) \dot{\mathbf{D}}_{k-1} - \left(\frac{\Delta t^2}{2} \mathbf{K}_k^i\right) \ddot{\mathbf{D}}_{k-1} \tag{7}$$

Equation (5) requires an iterative solving, at each time step k, to correct the tangent stiffness matrix $\mathbf{K}_k^i$. Starting from the stiffness matrix $\mathbf{K}_k^1 = \mathbf{K}_{k-1}$, evaluated at the previous time step, the value of matrix $\mathbf{K}_k^i$ is updated at each iteration i (Crisfield 1991). An elastic behavior is assumed for the first iteration at the first time step.

Three terms in the vector of acceleration increments $\Delta \ddot{\mathbf{D}}_k^i$ are known, that is, the first term of each of three n-dimensional subvectors corresponds to the imposed borehole acceleration at node 1 in x-, y- and z-direction of motion. Organizing rows and columns of equation (5) to separately group borehole and unknowns parameters of motion (index b and u, respectively), according to

$$\begin{bmatrix} \bar{\mathbf{M}}_{bb} & \bar{\mathbf{M}}_{bu} \\ \bar{\mathbf{M}}_{ub} & \bar{\mathbf{M}}_{uu} \end{bmatrix}_k^i \begin{bmatrix} \Delta \ddot{\mathbf{D}}_b \\ \Delta \ddot{\mathbf{D}}_u \end{bmatrix}_k^i = \begin{bmatrix} \mathbf{A}_b \\ \mathbf{A}_u \end{bmatrix}_k^i \tag{8}$$

the unknown acceleration increments are evaluated consequently, as

$$\left[\Delta \ddot{\mathbf{D}}_u\right]_k^i = \left[\bar{\mathbf{M}}_{uu}^{-1}\right]_k^i \left(\left[\mathbf{A}_u\right]_k^i - \left[\bar{\mathbf{M}}_{ub}\right]_k^i \left[\Delta \ddot{\mathbf{D}}_b\right]_k^i\right) \tag{9}$$

After evaluating the unknown acceleration increment $\left[\Delta \ddot{\mathbf{D}}_u\right]_k^i$, at all nodes except the first one, by equation (9), using the tangent stiffness matrix corresponding to the current time step, and then the acceleration increment vector $\Delta \ddot{\mathbf{D}}_k^i$, the total motion is obtained according to Newmark's procedure as

$$\begin{cases} \ddot{\mathbf{D}}_k^i = \ddot{\mathbf{D}}_{k-1} + \Delta \ddot{\mathbf{D}}_k^i \\ \dot{\mathbf{D}}_k^i = \left(\dot{\mathbf{D}}_{k-1} + \Delta t\left(1-\alpha\right)\ddot{\mathbf{D}}_{k-1}\right) + \alpha\,\Delta t\,\ddot{\mathbf{D}}_k^i \\ \mathbf{D}_k^i = \left(\mathbf{D}_{k-1} + \Delta t\,\dot{\mathbf{D}}_{k-1} + \dfrac{\Delta t^2}{2}\left(1-2\beta\right)\ddot{\mathbf{D}}_{k-1}\right) + \beta\,\Delta t^2\,\ddot{\mathbf{D}}_k^i \end{cases} \tag{10}$$

where $\mathbf{D}_k^i$, $\dot{\mathbf{D}}_k^i$ and $\ddot{\mathbf{D}}_k^i$ are the vectors of total displacement, velocity and acceleration, respectively. The two parameters $\beta = 0.3025$ and $\alpha = 0.6$ guarantee unconditional stability of the time integration scheme and numerical damping properties to damp higher modes (Hughes 1987).

The strain increments are then derived from the displacement increments $\mathbf{D}_k^i - \mathbf{D}_{k-1}$. Stress increments and tangent constitutive matrix are obtained through the assumed constitutive relationship. Gravity load is imposed as static initial condition in terms of strain and stress at nodes. The stiffness matrix $\mathbf{K}_k^i$ and the modified mass matrix $\bar{\mathbf{M}}_k^i$ are then calculated and the process restarts. The correction process continues until the difference between two successive approximations is reduced to a fixed tolerance, according to

$$\left|\mathbf{D}_k^i - \mathbf{D}_k^{i-1}\right| < \eta \left|\mathbf{D}_k^i\right| \tag{11}$$

where $\eta = 10^{-3}$ (Mestat 1993, 1998). Afterwards, the next time step is analyzed.

2.4 Boundary conditions

The system of horizontal soil layers is bounded at the top by the free surface and the stresses normal to it are assumed null.

The largely adopted absorbing boundary condition at the soil-bedrock interface, proposed by Joyner & Chen (1975), is used in a 1D-3C wave propagation model by Santisi d'Avila *et al*. (2012, 2013). Some rock type profiles are selected close to each analyzed soil column and the halved signal recorded at these rock outcrops are applied as 3C incident wave. Computed and recorded motions at the surface of analyzed soil profile are compared to validate the 1D-3C model. A great variability of the seismic response is observed at the surface of soil profiles, with the selected bedrock motion. The accuracy of the predicted soil motion depends significantly on the rock motion characteristics. The lack of geotechnical data could induce to questionable results when the geological homogeneity of selected rock type outcrops and the modeled bedrock, underlying analyzed soil profiles, is not assessed.

When borehole records are used, the motion at the soil-bedrock interface (node 1 in Fig. 1), containing incident and reflected waves, is known and directly imposed as boundary condition. The soil and quake properties are related to the same stratigraphy, increasing the accuracy of results. Borehole records are imposed in terms of three-component accelerations at node 1 of the finite element scheme.

3 SOIL PROPERTIES AND QUAKE FEATURES

Recorded data from the 11 March 2011 Mw 9 Tohoku earthquake stored by the Kiban-Kyoshin Network (KiK-Net) accelerometer network have been analyzed in this research, to numerically reproduce the ground motion at the surface and to provide profiles with depth of mechanical and motion parameters. The KiK-Net database stores surface and borehole seismic records for different stratigraphies.

Records at the surface of some selected alluvial soil profiles (Fig. 2) are used to validate the numerical surface ground motion computed by the proposed 1D-3C model, by using the borehole records as inputs, imposed as boundary condition at the base of the soil profiles. The validation is done using records at the ground surface, since it is the only available motion record. Figure 2

3.1 Soil profiles

The stratigraphic setting of four soil profiles in the Tohoku area (Japan) is used in this analysis (Fig. 2). The description of the stratigraphy and lithology of these alluvial deposits is provided by the KiK-Net database. Epicentral distances are listed in Table 1. Analyzed profiles have been selected between stratigraphies proposed by KiK-Net, adopting as criteria the choice of soil type profiles and a high vertical to horizontal component ratio of the ground motion measured at their surface. Soil profiles have different properties: depth *H*, number and thickness of layers *N*, average shear wave velocity $v_s = H \Big/ \sum_{j=1}^{N} H_j / v_{s\,j}$, soil type and seismic velocity ratio (compressional to shear wave velocity ratio v_p / v_s) that is related to the Poisson's ratio (Table 1). Stratigraphies used in this analysis and soil properties of each layer *j*, as thickness H_j, shear and pressure wave velocity in the medium, density ρ and the reference shear strain γ_r, are shown in

Tables 2-5. Soil properties are assumed homogeneous in each layer. Table 1

The nonlinear mechanical properties of the Tohoku alluvial deposits are not provided. The normalized shear modulus decay curves employed in this work are obtained according to the hyperbolic model. The applied reference shear strain γ_r corresponds, for each soil type in the analyzed profiles, to an actual tangent shear modulus equivalent to 50 % of the initial shear modulus, in a normalized shear modulus decay curves of the literature (Tables 2-5). Curves proposed by Seed & Idriss (1970) are used to define the reference strain for sands and the curve of Seed & Sun (1989) is applied for clays. A plasticity index in the range of $\mathrm{PI} = 5 - 10$ is assumed in the relationship of Sun *et al*. (1988) to define the reference strain for silt. The reference shear strain for gravel is defined according to Seed *et al*. (1986). An almost linear behavior is assumed for stiff layers (γ_r = 100 ‰).

The density of soil layers is not even provided by the KiK-Net database, consequently it is assumed, based on density range for each soil type.

Tables 2, 3, 4, 5

3.2 Seismic excitations

The 2011 Tohoku earthquake is one of the largest earthquakes in the world that has been well recorded in the near-fault zone. The vertical to maximum horizontal component ratio appears close to one for several soil profiles and the peak vertical motion can locally be higher than the minor horizontal component of ground motion. The four analyzed soil profiles have been selected because having a high vertical to horizontal peak ground acceleration ratio (Table 1) during the 11 March 2011 Mw 9 Tohoku earthquake. The peak ground acceleration (PGA) recorded at the surface of analyzed soil profiles is higher than the acceleration level commonly used for structural design in high risk seismic zones. The three components of motion are recorded in North-South (NS), East-West (EW) and Up-Down (UP) directions, respectively referred to as x, y and z in the proposed model. Recorded signals have different polarizations. The three maximum acceleration components, in each direction of motion, correspond to different time instants. Peaks of the three components of motion at the base and surface of analyzed soil profiles are synthetized in Tables 6 and 7, respectively. The waveforms are provided by the KiK-Net strong ground motion database. Borehole seismic records are measured at various depths (Table 1). Table 6, 7

Three-component seismic signals recorded downhole in directions NS, EW and UD, during the 2011 Tohoku earthquake (Table 6), are propagated in the various soil columns. The three components induce shear loading in horizontal directions x (NS) and y (EW) and pressure loading in z -direction (UD).

Downhole and surface recorded time histories, in terms of acceleration modulus, are compared in Fig. 3 to show the strong amplification effects in these alluvial deposits. Vertical to maximum horizontal component ratios are indicated in Table 1. Figure 3

In this research, the maximum frequency is imposed as $f = 10\,\mathrm{Hz}$ and the minimum shear velocity in the soil v_s is $150\,\mathrm{m/s}$ (Table 2) then, the minimum number of nodes per wavelength r is always higher than 10 in all the analyzed cases, to accurately represent the seismic signal.

4 1D-3C LOCAL SEISMIC RESPONSE ANALYSIS OF THE TOHOKU AREA

The local dynamic response of analyzed soil profiles to the one-directional seismic wave propagation is presented, validated and discussed.

4.1 Validation of the 1D-3C model by GoF criteria

Numerical acceleration and velocity time histories appear consistent with recordings in Figs 4-7. Nevertheless, the goodness of synthetic seismograms must be confirmed by comparing statistical characteristics.

The validation of the proposed model and numerical procedure is done by comparison of computed results with records using Anderson's Goodness of Fit (GoF) criteria (Anderson 2004). Quantitative scores proposed by Anderson are estimated to characterize the GoF of 1D-3C synthetics. According to him, the agreement between records and numerical results are classified as poor fit if the score is below 4 over 10, fair fit in the range 4/10 - 6/10, good fit for 6/10 - 8/10 and excellent fit for scores higher than 8 over 10. The error is measured as follows:

$$S\left(p_n, p_r\right) = 10\exp\left(-\left(\frac{p_n - p_r}{\min\left(p_n, p_r\right)}\right)^2\right) \qquad (12)$$

where p_n and p_r are evaluated parameters for numerical seismograms and records, respectively. Records and numerical signals shown in following figures are band-pass filtered between 0.05 and 10 Hz. The whole band of frequency is analyzed in the comparisons.

The seismograms are adequately fitted in terms of peak acceleration and peak velocity that are listed in Table 7, for the three components of motion at the surface of the four analyzed soil profiles. Bold characters indicate measured PGA. Records are band-pass filtered in the same frequency band as synthetics to allow comparisons. Signals in Fig. 4 (MYGH09) show excellent fit (over 9) for horizontal components, in terms of acceleration, and a good fit for the vertical component. Velocities provide an excellent fit for the three components. Synthetics in Fig. 5 (FKSH20) show an excellent fit of *x*-component and poor and fair fit for *y*- and *z*-component, respectively. Instead, *x*- and *z*-velocities are excellently fitted and *y*-velocity is well fitted.

Seismograms in Fig. 6 (IWTH04) show clearly an excellent fit for horizontal accelerations and velocities and a fair and poor fit for *z*-direction, in terms of velocity and acceleration, respectively. Records at the surface of soil profile IBRH12 (Fig. 7) obtain excellent and good scores for horizontal accelerations and three components of velocity and a fair score for vertical acceleration. Comparing the peak displacement of seismograms, we obtain a great variability of scores. Grades for peak acceleration (PA), peak velocity (PV) and peak displacement (PD) are evaluated according to Anderson's criterion (12) and listed in Table 8. Figures 4, 5, 6, 7

A comparison of peaks is incomplete to guarantee the GoF of synthetic seismograms. Analyzing other parameters suggested by Anderson (2004), like the shape of the normalized integrals of acceleration and velocity squared, normalized with respect to Arias intensity and the energy integral respectively, we observe excellent fit for MYGH09 (Fig. 8), good and excellent fit for various components at the surface of FKSH20, IWTH04 and IBRH12 profiles (see NIA and NIE columns in Table 8). The energy integral is the integral of velocity squared for the complete duration of the accelerogram.

Verifying the values used for normalization, that are the Arias intensity (IA) and the energy integral (IE), the error reaches different scores (Table 8). The scores confirm the differences remarked in acceleration and velocity time histories. Fitting of *z*-component is often the most difficult. See for example the case of IWTH04 profile (Fig. 6), with vertical to horizontal component ratio greater than 1. This raises the question of whether compressive behavior is properly modeled when a multiaxial loading is applied with a high pressure component. Figure 8

Finally, we observed acceleration response and Fourier spectra. A 5% damping is assumed to derive the acceleration response spectrum. According to Anderson (2004), the score related to the Fourier spectrum and the cross-correlation in the whole band of frequency are lower than others (see FFT and CC columns in Table 8). A poor fit is obtained in all cases. Instead, an excellent fit is attained, in terms of acceleration response spectrum, for the maximum horizontal and vertical components in MYGH09, the *x*-component in FKSH20, both horizontal components in IWTH04 and the *y*-component in IBRH12. Fair fits are obtained in other cases (see SA column in Table 8). Best fitted spectra, for each soil profile, are reproduced in Fig. 9, where seismic response amplification from the bottom to the surface can be observed in terms of acceleration response spectrum. Figure 9

The lack of data about soil properties, such as density and $G(\gamma)$, demands future studies to analyze if the results could be improved when all measurable data are available. The choice of density and shear modulus decay curve, for each soil layer, strongly influence the analysis, modifying, respectively, the initial elastic properties and material behavior at larger strains. Furthermore, amplification effects at the surface of soil profiles and energy spectra are modified not only by soil properties of each individual layer, but especially by the combination of seismic impedances of various soil layers. Soil profile layering complicating the issue, measured soil properties used for all input data in the numerical model would lead to more reliable results. In particular when various layers are modeled (12 layers in MYGH09, 28 in IBRH12), a great variability of results can be obtained with different assumptions for density and reference shear strain of each layer. The benchmark Prenolin, as part of Cashima research project, will provide measured soil and quake data for some study cases and will allow to adjust 1D seismic wave propagation models. Table 8

4.2 Local dynamic response of soil profiles

The proposed model allows to study the local seismic response in case of strong earthquakes affecting alluvial sites and assess possible amplifications of seismic motion at the surface, influenced by stratigraphic characteristics. Non-measured parameters of motion, stress and strain along the soil profiles can be computed, in order to investigate nonlinear effects in deeper details. Modeling the one-directional propagation of a three-component earthquake allows to take into account the interactions between shear and pressure components of the seismic load. Nonlinear and multiaxial coupling effects appear under a triaxial stress state induced by a cyclic 3D loading. The interaction between multiaxial stresses in the 3C approach allows to reproduce energy dissipation effects that yields a reduction of the ground motion at the surface, compared with the approach considering the superposition of three one-component propagations.

4.2.1 Response with depth

The seismic response of soil profiles MYGH09, FKSH20, IWTH04 and IBRH12, to the propagation of a three-component signal (1D-3C approach), is analyzed in terms of depth profiles of maximum acceleration and velocity of each component of motion and maximum shear stress and strain and in terms of shear stress-strain loops in the most deformed layer (Figs 10-13). Stratigraphies and soil properties are given in Tables 2-5. The profile of maximum motion vs depth shows, at each z -coordinate, the peak of the ground motion during shaking. The same criterion is adopted for strain and stress profiles. The maximum acceleration profiles with depth are displayed in all these figures without low-pass filtering operations.

Parameters of motion, stress and strain along the analyzed soil profiles, evaluated by the 1D-3C approach, are influenced by the input motion polarization and 3D loading path. Both shear stresses, τ_{yz} and τ_{zx}, and non-zero normal stress components σ_{xx}, σ_{yy} and σ_{zz} are assessed along the soil profile, consequence of the three strains in z -direction, γ_{yz}, γ_{yz} and ε_{zz}.

Soft layers and high strain jumps at layer interfaces can be identified evaluating the maximum strain profiles with depth. We observe that maximum strains along the soil profile are located at layer interfaces (Figs 10a, 11a, 12a and 13).

The wave polarization is modified along the depth. The PGA does not correspond to the same horizontal component all along the soil profile. Since polarization changes along the depth, at a given depth, nonlinear effects and strain level are more important for the maximum peak horizontal component at this depth and not for the direction of measured PGA at the ground surface (see hysteresis loop for the minimum horizontal component at the surface in Figs 10 and 12).

Figures 10, 11, 12, 13

4.2.2 Hysteresis loops

Cyclic shear strains with amplitude higher than the elastic behavior range limit give open loops in the shear stress-shear strain plane, exhibiting strong hysteresis. Due to nonlinear effects, the shear modulus decreases and the dissipation increases with increasing strain amplitude. In the case of one-component loading, the shape of the first loading curve is the same as the backbone curve and the shape of hysteresis loops remains unvaried at each cycle, for shear strains in the range of stable nonlinearity (Santisi d'Avila *et al.* 2012). In the case of three-component loading, the shape of the hysteresis loops changes at each cycle, even in a strain range corresponding to stable nonlinearity in the 1C case. The shape of the loops is indeed disturbed by the multiaxial stress coupling. Under triaxial loading the material strength is lower than for simple shear loading, referred to as the backbone curve. The cyclic response of the soil column in terms of shear stress and strain, when it is excited by a triaxial input signal (1D-3C), is shown in Figs 10b-12b. The shape of the shear stress-strain cycles in x -direction (respectively y -direction) reflects the coupling effects with loads in directions y (respectively x) and z. Hysteresis loops for each horizontal direction are altered as a consequence of the interaction between loading components. The strain level reached in the stiff IBRH12 profile is low, with closely linear behavior.

We detect, in all hysteresis loops (Figs 10b-12b), two successive events which is a feature of the 2011 Tohoku earthquake (Bonilla *et al*. 2011). Observing Figs 4-7, these two successive events can be easily distinguished, confirming the reliability of the proposed model.

4.2.3 Component ratio vs time

Fig. 14 shows the seismic wave polarization with time, at the surface of the analyzed soil profiles, in terms of acceleration. The 3D polarization is represented by a unit vector, whose components are $\bar{a}_x$, $\bar{a}_y$ and $\bar{a}_z$, with respect to *x*-, *y*- and *z*-axis respectively. Acceleration parameters $\bar{a}_x = a_x / |a|$, $\bar{a}_y = a_y / |a|$ and $\bar{a}_z = a_z / |a|$ are the normalized acceleration components with respect to acceleration modulus $|a|$. The three shares $\left(\bar{a}_x^{\,2} \big/ \sqrt{\bar{a}_x^{\,2} + \bar{a}_y^{\,2}}\right)\cos\alpha$, $\left(\bar{a}_y^{\,2} \big/ \sqrt{\bar{a}_x^{\,2} + \bar{a}_y^{\,2}}\right)\cos\alpha$ and $|\bar{a}_z|\sin\alpha$ are the projections of the three normalized acceleration components $\bar{a}_x$, $\bar{a}_y$ and $\bar{a}_z$, respectively, in the wave propagation direction (the direction of the unit vector), as a consequence their sum is equal to one. The angle θ, such as $\tan\theta = |\bar{a}_z| \big/ \sqrt{\bar{a}_x^{\,2} + \bar{a}_y^{\,2}}$, is the projection angle of the unit vector in *xy* horizontal plane. The representation of normalized acceleration contribution for the three components of motion, during the total duration of numerical and recorded seismograms, is shown in Fig. 14.

Figure 14

The variability of the contribution of each component of motion with time is an interesting result, to assess the reliability of the proposed 1D-3C model. The direction of the PGA (Max SH in Fig.

14) does not correspond to the maximum acceleration direction all along the signal duration. The direction of maximum horizontal component of motion changing with time, as well as the importance of the vertical component (P in Fig. 14), confirm the interest of taking into account the three-component coupling in 1D wave propagation models. Unsteady results are obtained for very low acceleration rates at the earthquake starting. This could be justified by the fact that the constitutive soil model is not calibrated for very small strain levels.

5 CONCLUSIONS

A one-dimensional three-component (1D-3C) approach, allowing to analyze the propagation along 1D soil profiles of 3C seismic waves, recorded downhole, is proposed, validated and discussed.

A three-dimensional constitutive relation of the Masing-Prandtl-Ishlinskii-Iwan (MPII) type, for cyclic loading, is implemented in a finite element scheme, modeling a horizontally multilayered soil. This constitutive model has been selected because emulating a 3D behavior, nonlinear for both loading and unloading, and, above all, because few parameters are necessary to characterize the soil hysteretic behavior.

Borehole records from 2011 Tohoku earthquake are used as 3C seismic excitations, imposed as a boundary condition at the base of the stacked horizontal soil layers.

The influence of the quake features and site-specific seismic hazard can be investigated by such a model. The soil and quake properties being associated to the same soil profile allows to perform quantitative analyses with acceptable accuracy.

The validation of the 1D-3C approach from recorded time histories is presented in this paper for four soil profiles in the Tohoku area (Japan), shaken by the 11 March 2011 Mw 9 Tohoku earthquake. Anderson's criteria are applied to assess the reliability of numerical seismograms. Synthetics adequately reproduce the records. In particular for the 2011 Tohoku earthquake, the two successive events, detected by records, are numerically replicated. The lack of measured data justifies the assumption of some soil properties (density and shear modulus decay curve) according to the literature. This demands future studies, to analyze if results are improved in cases where all measurable data are available.

The effects of the input motion polarization and 3D loading path can be detected by the 1D-3C approach. It allows to evaluate non-measured parameters of motion, stress and strain along the analyzed soil profiles, in order to detail nonlinear effects and the influence of soil profile layering on local seismic response. Maximum strains are induced at layer interfaces, where waves encounter large variations of impedance contrast, along the soil profile.

The wave polarization is modified along the propagation path. The PGA does not correspond to the same horizontal component all along the soil profile. For this reason, at a given depth, nonlinear effects and strain level are more important for the maximum peak horizontal component at this depth and not for the direction of measured PGA at the ground surface.

A low seismic velocity ratio in the soil and a high vertical to horizontal component ratio increase the three-dimensional mechanical interaction and progressively change the hysteresis loop size and shape at each cycle, even in a strain range of stable nonlinearity in the 1C case.

The variability of the propagating wave polarization with time and the significant contribution of vertical component confirm the importance of taking into account the three component coupling in 1D wave propagation models.

The extension of this approach to higher strain rates, considering the consequences of soil nonlinearity in saturated conditions, would be a natural improvement of the proposed 1D-3C model.

Statistical studies using records of different earthquakes at a same site could be undertaken using the 1D-3C approach, for the evaluation of local seismic response for site effect analyses.

ACKNOWLEDGMENTS

Seismograms and soil stratigraphic setting used in this study are provided by the National research Institute for Earth science and Disaster prevention (NIED), in Japan, and can be obtained from the Kiban-Kyoshin Network at www.k-net.bosai.go.jp (last accessed January 2013).

We thank Mario Ordaz for providing Degtra software, developed by the Universidad National Autonoma de Mexico.

REFERENCES

Anderson, J.G., 2004. Quantitative measure of the goodness-of-fit of synthetic seismograms, *13th World Conference on Earthquake Engineering*, Paper no. 243, Vancouver, Canada.

Assimaki, D., Li W. & Kalos A., 2011. A wavelet-based seismogram inversion algorithm for the in situ characterization, *Pure Appl. Geophys*., 168, 1669–1691.

of Nonlinear Soil Behavior

Bard, P.Y. & Bouchon E.T., 1985. Underground and ridge site effects: a comparison of observation and theory, *Bull. Seism. Soc. Am.*, 75, 905–922.

Bardet, J.P., Ichii K., & Lin C.H., 2000. *EERA: A computer program for Equivalent-linear Earthquake site Response Analyses of layered soil deposits*, University of Southern California, United States.

Bardet, J.P. & Tobita T., 2001. *NERA: A computer program for Nonlinear Earthquake site Response Analyses of layered soil deposits*, University of Southern California, United States.

Batoz J.L. & Dhatt G., 1990. *Modélisation des structures par éléments finis*, Vol. 1, Hermes, Paris, France.

Bertotti, G. & Mayergoyz I., 2006. *The science of hysteresis: mathematical modeling and applications*, Elsevier, Amsterdam, Netherlands, 1–114.

Bonilla, L.F., Tsuda K., Pulido N., Régnier J., & Laurendeau A., 2011. Nonlinear site response evidence of K-Net and KiK-Net records from the 2011 off the Pacific coast of Tohoku Earthquake, *Earth Planets Space*, 63, 785–789.

Cook R.D., Malkus D.S., Plesha M.E. & Witt R.J., 2002. *Concepts and applications of finite element analysis*, 4th edn, John Wiley & Sons, New York, United States.

Crisfield, M.A., 1991. *Non-linear finite element analysis of solids and structures*, Vol. 1, John Wiley and Sons, Chichesrter, England, 8–55.

Delépine, N., Bonnet G., Lenti L. & Semblat J.F., 2009. Nonlinear viscoelastic wave propagation: an extension of Nearly Constant Attenuation models, *J. Eng. Mech*., 135(11), 1305–1314.

Hardin, B.O., & Drnevich V.P., 1972. Shear modulus and damping in soil: design equations and curves, *J. Soil Mech. Found. Div.*, 98, 667–692.

Hashash Y.M.A. & Park D., 2001. Non-linear one-dimensional seismic ground motion propagation in the Mississippi embayment, *Eng. Geology*, 62(1–3), 185–206.

Hilber, H.M., Hughes T.J.R., & Taylor R.L., 1977. Improved numerical dissipation for time integration algorithms in structural dynamics, *Earthquake Eng. Struct. Dyn.*, 5, 283–292.

Hughes, T.J.R., 1987. *The finite element method - Linear static and dynamic finite element analysis*, Prentice Hall, Englewood Cliffs, New Jersey, 490–567.

Iwan, W.D., 1967. On a class of models for the yielding behavior of continuous and composite systems, *J. Appl. Mech.*, 34, 612–617.

Joyner, W., 1975. A method for calculating nonlinear seismic response in two dimensions, *Bull. Seism. Soc. Am.*, 65(5), 1337–1357.

Joyner, W.B., & Chen A.T.F., 1975. Calculation of nonlinear ground response in earthquakes, *Bull. Seism. Soc. Am.*, 65(5), 1315–1336.

Kausel, E., & Assimaki, D., 2002. Seismic Simulation of Inelastic Soils via Frequency-Dependent Moduli and Damping, *J. Eng. Mech*., 128(1), 34–47.

Lee, K.W., & Finn W.D.L., 1978. DESRA-2: Dynamic effective stress response analysis of soil deposits with energy transmitting boundary including assessment of liquefaction potential, in *Soil Mechanics Series*, University of British Columbia, Vancouver, Canada.

Li, X.S., 1990. *Free field response under multidirectional earthquake loading*, PhD thesis, University of California, Davis, United States.

Li, X.S., Wang Z.L., & Shen C.K., 1992. *SUMDES: A nonlinear procedure for response analysis of horizontally-layered sites subjected to multi-directional earthquake loading*, University of California, Davis, United States.

Matasovic N., 2006. *D-MOD_2: A Computer Program for Seismic Response Analysis of Horizontally Layered Soil Deposits, Earthfill Dams, and Solid Waste Landfills. User's Manual*, GeoMotions, LLC, Washington.

Mestat, P., 1993. Lois de comportement des géomatériaux et modélisation par la méthode des éléments finis, in *Etudes et recherches des Laboratoires des Ponts et Chaussées*, Geotechnical Series, GT52, Paris, France.

Mestat, P., 1998. Modèles d'éléments finis et problèmes de convergence en comportement non linéaire, *Bull. Lab. Ponts Chaussées*, 214, 45–60.

Newmark, N.M., 1959. A method of computation for structural dynamics. *J. Eng. Mech.*, 85(EM3), 67–94.

Oppenheim, A.V., Willsky A.S., & Nawab S.H., 1997. *Signals and systems,* 2nd edn, Prentice Hall, Upper Saddle River, New Jersey, 53–56.

PEERC, 2008. *Benchmarking of nonlinear geotechnical ground response analysis procedures*, PEER Report 2008/04, University of California, Berkeley, United States.

Reddy J. N., 1993. *An introduction to the finite element method*, 2nd edn, Mac Graw Hill, Hightstown, New Jersey.

Santisi d'Avila M.P., Lenti L., & Semblat J.F., 2012. Modeling strong seismic ground motion: 3D loading path vs wavefield polarization, *Geophys. J. Int.*, 190, 1607–1624.

Santisi d'Avila M.P., Semblat J.F. & Lenti L., 2013. Strong Ground Motion in the 2011 Tohoku Earthquake: a 1Directional - 3Component Modeling, *Bull. Seism. Soc. Am.*, Special issue on the 2011 Tohoku Earthquake, 103(2b).

Schnabel, P.B., Lysmer J., & Seed H.B., 1972. SHAKE: A computer program for earthquake response analysis of horizontally layered sites, *Report UCB/EERC-72/12*, Earthquake Engineering Research Center, University of California, Berkeley, United States.

Seed, H.B., & Idriss I.M., 1970. Soil moduli and damping factors for dynamic response analyses, *Report UCB/EERC-70/10*, Earthquake Engineering Research Center, University of

California, Berkeley, United States.

Seed, H.B., & Sun J.I., 1989. Implication of site effects in the Mexico City earthquake of September 19, 1985 for Earthquake-Resistant Design Criteria in the San Francisco Bay Area of California, *Report UCB/EERC-89/03*, Earthquake Engineering Research Center, University of California, Berkeley, United States.

Seed H.B., Wong R.T., Idriss I.M., & Tokimatsu K., 1986. Moduli and damping factors for dynamic analyses of cohesionless soils, *Report UCB/EERC-84/14*, Earthquake Engineering Research Center, University of California, Berkeley, United States.

Segalman, D.J., & Starr M.J., 2008. Inversion of Masing models via continuous Iwan systems, *Int. J. Nonlinear Mech.*, 43, 74–80.

Semblat, J.F. & Pecker A., 2009. *Waves and vibrations in soils*, IUSS Press, Pavia, Italy.

Sun, J.I., Golesorkhi R., & Seed H.B., 1988. Dynamic moduli and damping ratios for cohesive soils, *Report UCB/EERC-88/15*, Earthquake Engineering Research Center, University of California, Berkeley, United States.

Viet Anh, P., Lenti L., Bonilla F., Semblat J.F. & Santisi d'Avila M.P., 2013. Réponse sismique non linéaire des sols et influence de la pression interstitielle, *French Conference on Mechanics*, Bordeaux, France.

Wang, Z.L., Dafalias Y.F., & Shen C.K., 1990. Bounding surface hypoelasticity model for sand, *J. Eng. Mech.*, 116, 5, 983–1001.

FIGURE LEGENDS

Figure 1. Spatial discretization of a horizontally layered soil excited at its base (node 1) by a three-component borehole seismic record.

Figure 2. Location of analyzed soil profiles in the Tohoku area (Japan), KiK-Net accelerometers being placed at the surface and at depth.

Figure 3. Time history of measured acceleration modulus at the base and surface of soil profiles MYGH09 (a), IWTH04 (b), FKSH20 (c) and IBRH12 (d), during the 2011 Tohoku earthquake.

Figure 4. Time history of measured and numerical acceleration (top) and velocity (bottom), in directions NS (left), EW (middle) and UD (right), at the surface of soil profile MYGH09, during the 2011 Tohoku earthquake.

Figure 5. Time history of measured and numerical acceleration (top) and velocity (bottom), in directions NS (left), EW (middle) and UD (right), at the surface of soil profile FKSH20, during the 2011 Tohoku earthquake.

Figure 6. Time history of measured and numerical acceleration (top) and velocity (bottom), in directions NS (left), EW (middle) and UD (right), at the surface of soil profile IWTH04, during the 2011 Tohoku earthquake.

Figure 7. Time history of measured and numerical acceleration (top) and velocity (bottom), in directions NS (left), EW (middle) and UD (right), at the surface of soil profile IBRH12, during the 2011 Tohoku earthquake.

Figure 8. Normalized integral of acceleration (top) and velocity (bottom) squared for soil profile MYGH09.

Figure 9. Numerical best fitted spectra, for soil profiles MYGH09 (a), IWTH04 (b), FKSH20 (c) and IBRH12 (d), and spectra corresponding to records at the bottom and at the surface.

Figure 10. 1D-3C seismic response of soil profile MYGH09, during the 2011 Tohoku earthquake, in both horizontal directions of motion: acceleration, velocity, strain and stress with depth (a); shear stress-strain loops at 2 m depth (b).

Figure 11. 1D-3C seismic response of soil profile FKSH20, during the 2011 Tohoku earthquake, in both horizontal directions of motion: acceleration, velocity, strain and stress with depth (a); shear stress-strain loops at 31 m depth (b).

Figure 12. 1D-3C seismic response of soil profile IWTH04, during the 2011 Tohoku earthquake, in both horizontal directions of motion: acceleration, velocity, strain and stress with depth (a); shear stress-strain loops at 4 m depth (b).

Figure 13. 1D-3C seismic response of soil profile IBRH12, during the 2011 Tohoku earthquake, in both horizontal directions of motion: acceleration, velocity, strain and stress with depth.

Figure 14. Recorded (top) and numerical (bottom) normalized polarization of seismic waves in terms of acceleration at the surface of soil profiles MYGH09 (a), FKSH20 (b), IWTH04 (c) and IBRH12 (d). Max SH is the PGA horizontal direction and P is the vertical direction.

TABLES

Table 1. Selected soil profiles in the Tohoku area (Japan)

Site name - Prefecture	Site code	Epicentral distance (km)	Depth H (m)	Average v_s ($m\ s^{-1}$)	a_z / PGA (%)	min $\{v_p / v_s\}$
SHIROISHI - MIYAGIKEN	MYGH09	198	100	560	90	2.42
NAMIE - FUKUSHIMAKEN	FKSH20	178	109	479	40	3.00
SUMITA - IWATEKEN	IWTH04	175	106	934	101	1.74
DAIGO - IBARAKIKEN	IBRH12	265	200	974	92	1.76

Table 2. Stratigraphy and soil properties of profile MYGH09

MYGH09	H-z (m)	H_j (m)	v_s ($m\ s^{-1}$)	v_p ($m\ s^{-1}$)	ρ ($kg\ m^{-3}$)	γ_r (‰)
Sand with gravel	2	2	150	400	1800	0.200
	6	4	360	900	1800	0.200
Rock	20	14	360	1660	1900	100
	28	8	490	1660	1900	100
Silt	30.6	2.6	490	1660	1300	0.427
Rock	38	7.4	490	1660	1900	100
	48	10	770	2030	1900	100
Silt	64	16	770	2030	1300	0.427
Rock	80	16	770	2030	1900	100
	86.15	6.15	840	2030	1900	100
	94.27	8.12	840	2030	1900	100
Silt with sand	100	5.73	840	2030	1900	0.427

Table 3. Stratigraphy and soil properties of profile FKSH20

FKSH20	H-z (m)	H_j (m)	v_s (m s^{-1})	v_p (m s^{-1})	ρ (kg m^{-3})	γ_r (‰)
Clay	4	4	350	1500	1200	2.431
	12.3	8.3	350	1500	1200	2.431
Sand with gravel	32	19.7	350	1500	1500	0.368
	60	28	500	1500	1500	0.368
	62.4	2.4	610	1900	1500	0.368
Silt	88	25.6	610	1900	1300	0.427
Rock	109	21	610	1900	1900	100

Table 4. Stratigraphy and soil properties of profile IWTH04

IWTH04	H-z (m)	H_j (m)	v_s (m s^{-1})	v_p (m s^{-1})	ρ (kg/m^{-3})	γ_r (‰)
Clay	1	1	220	440	1200	2.431
Sand	5	4	220	440	1900	0.200
Clay	15	10	400	800	1200	2.431
Rock	49	34	830	2200	2100	100
	106	57	2300	4000	2100	100

Table 5. Stratigraphy and soil properties of profile IBRH12

IBRH12	H-z (m)	H_j (m)	v_s (m s^{-1})	v_p (m s^{-1})	ρ (kg/m^{-3})	γ_r (‰)
Rock	6	6	240	550	1700	100
	10	4	560	1900	1700	100
Sand with silt	14	4	560	1900	1550	0.368
Silt	16	2	560	1900	1350	0.427
Sand with silt	20	4	560	1900	1550	0.368
	26	6	850	2450	1550	0.368
Rock	32	6	850	2450	1900	100
Sand with silt	36	4	850	2450	1550	0.368
Rock	40	4	850	2450	1900	100
Silt	46	6	850	2450	1350	0.427
Rock	50	4	850	2450	1900	100
Sand with silt	56	6	850	2450	1550	0.368
Silt	58	2	850	2450	1350	0.427
Rock	74	16	1280	2650	2100	100
Silt	90	16	1120	2550	1350	0.427
Rock	92	2	1120	2550	2100	100
Silt	108	16	1120	2550	1350	0.427
Rock	112	4	1120	2950	2100	100
Silt	120	8	1120	2950	1350	0.427
Sand with silt	126	6	1120	2950	1550	0.368
Silt	136	10	1120	2950	1350	0.427
Rock	150	14	1450	2950	2100	100
Silt	154	4	1250	2700	1350	0.427
Sand with silt	158	4	1250	2700	1550	0.368
Silt	174	16	1250	2700	1350	0.427
Rock	195	21	1700	3000	2100	100
Silt	197	2	1700	3000	1350	0.427
Rock	203	6	1700	3000	2100	100

Table 6. Acceleration-components recorded downhole during the 2011 Tohoku earthquake

Site code	a_x ($m\ s^{-2}$)	a_y ($m\ s^{-2}$)	a_z ($m\ s^{-2}$)	a_z / PGA (%)
MYGH09	1.26	1.22	1.06	84
FKSH20	1.57	3.56	1.54	43
IWTH04	0.83	0.86	0.73	85
IBRH12	1.21	1.08	0.73	60

Table 7. Numerical and recorded acceleration and velocity components of the 2011 Tohoku earthquake at the surface of selected soil profiles

Site code		a_x ($m\ s^{-2}$)	a_y ($m\ s^{-2}$)	a_z ($m\ s^{-2}$)	v_x ($m\ s^{-1}$)	v_y ($m\ s^{-1}$)	v_z ($m\ s^{-1}$)
	Record	3.15	**3.23**	2.91	**0.31**	0.30	0.23
MYGH09	Filtered	3.05	**3.07**	2.22	**0.31**	0.30	0.23
	1D-3C	3.10	2.84	3.27	0.41	0.32	0.26
	Record	3.94	**6.60**	2.66	0.44	**1.09**	0.15
FKSH20	Filtered	3.90	**6.60**	2.21	0.44	**1.09**	0.15
	1D-3C	2.72	2.73	3.99	0.35	0.68	0.18
	Record	3.33	**3.84**	**3.88**	0.20	**0.24**	0.09
IWTH04	Filtered	3.10	**3.84**	**2.78**	0.20	**0.24**	0.09
	1D-3C	3.36	2.78	7.15	0.19	0.19	0.16
	Record	**6.04**	5.26	5.58	**0.29**	0.26	0.13
IBRH12	Filtered	**5.78**	5.25	4.31	**0.29**	0.26	0.13
	1D-3C	3.61	3.77	2.50	0.23	0.19	0.14

Table 8. Anderson's Good-of-Fit scores (NIA, shape of the normalized integral of acceleration squared with respect to Arias intensity; NIE, shape of the normalized integral of velocity squared with respect to the energy integral; IA, Arias intensity; IE, energy integral; PA, peak acceleration; PV, peak velocity; PD, peak displacement; SA, acceleration response spectrum; FFT, Fourier spectrum; CC, cross correlation) for numerical seismograms of the 2011 Tohoku earthquake at the surface of selected soil profiles : Excellent (A), Good (B), Fair (C), Poor (D)

Site code		NIA	NIE	IA	IE	PA	PV	PD	SA	FFT	CC
	x	A	A	D	C	A	A	D	C	D	D
MYGH09	y	A	A	D	A	A	A	B	A	D	D
	z	A	A	D	A	A	A	A	A	D	D
	x	A	A	A	C	A	A	D	A	D	D
FKSH20	y	A	C	A	D	D	B	D	D	D	D
	z	B	A	D	C	C	A	A	C	D	D
	x	A	A	D	A	A	A	D	A	D	D
IWTH04	y	B	A	D	A	A	A	A	A	D	D
	z	A	B	D	D	D	C	A	D	C	D
	x	A	A	C	A	B	A	D	B	D	D
IBRH12	y	A	A	A	B	A	A	D	A	D	D
	z	B	A	B	B	C	A	A	C	D	D

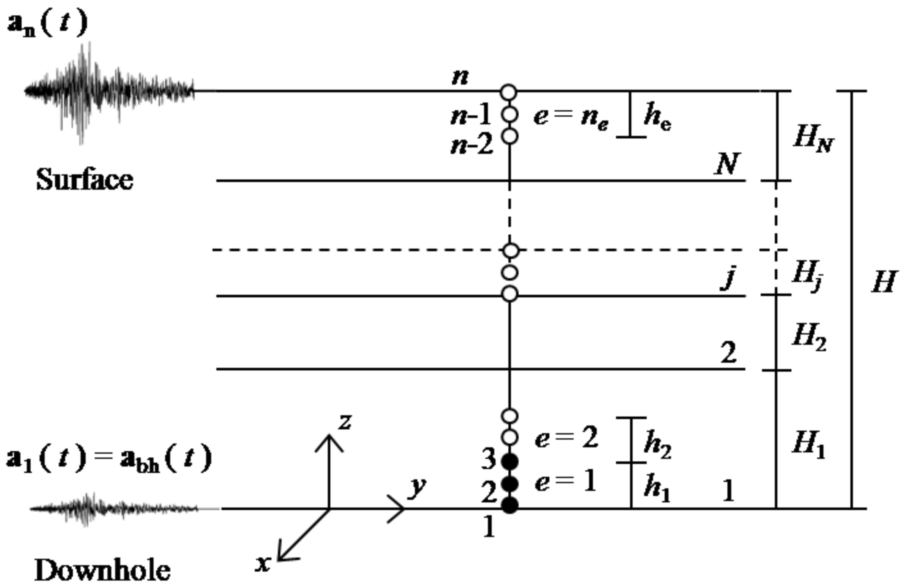

Figure 1. Spatial discretization of a horizontally layered soil excited at its base (node 1) by a three-component borehole seismic record.

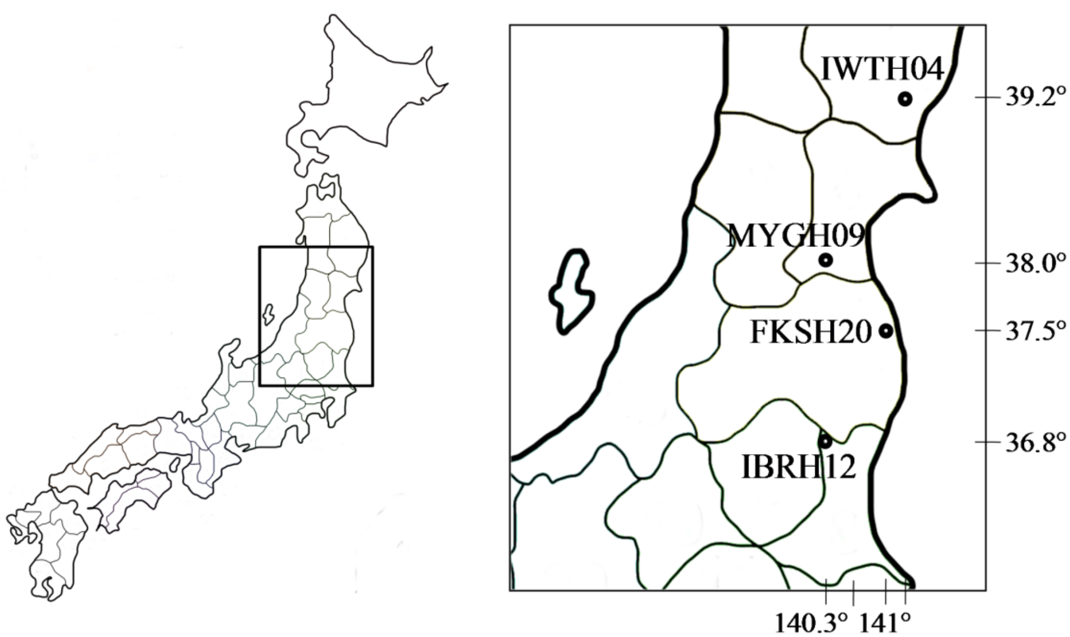

Figure 2. Location of analyzed soil profiles in the Tohoku area (Japan), KiK-Net accelerometers being placed at the surface and at depth.

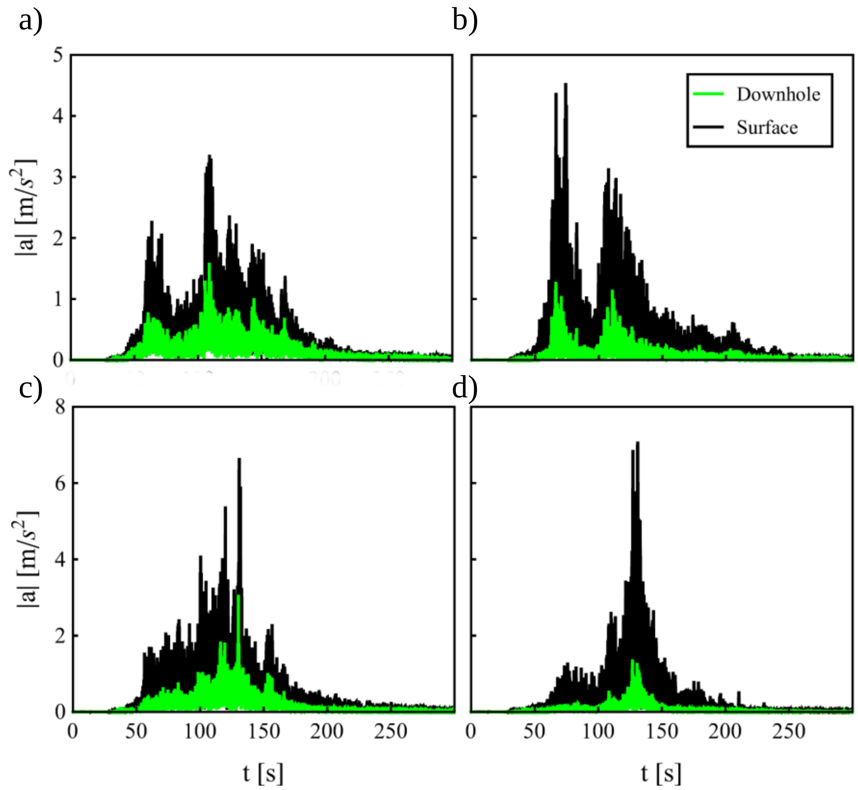

Figure 3. Time history of measured acceleration modulus at the base and surface of soil profiles MYGH09 (a), IWTH04 (b), FKSH20 (c) and IBRH12 (d), during the 2011 Tohoku earthquake.

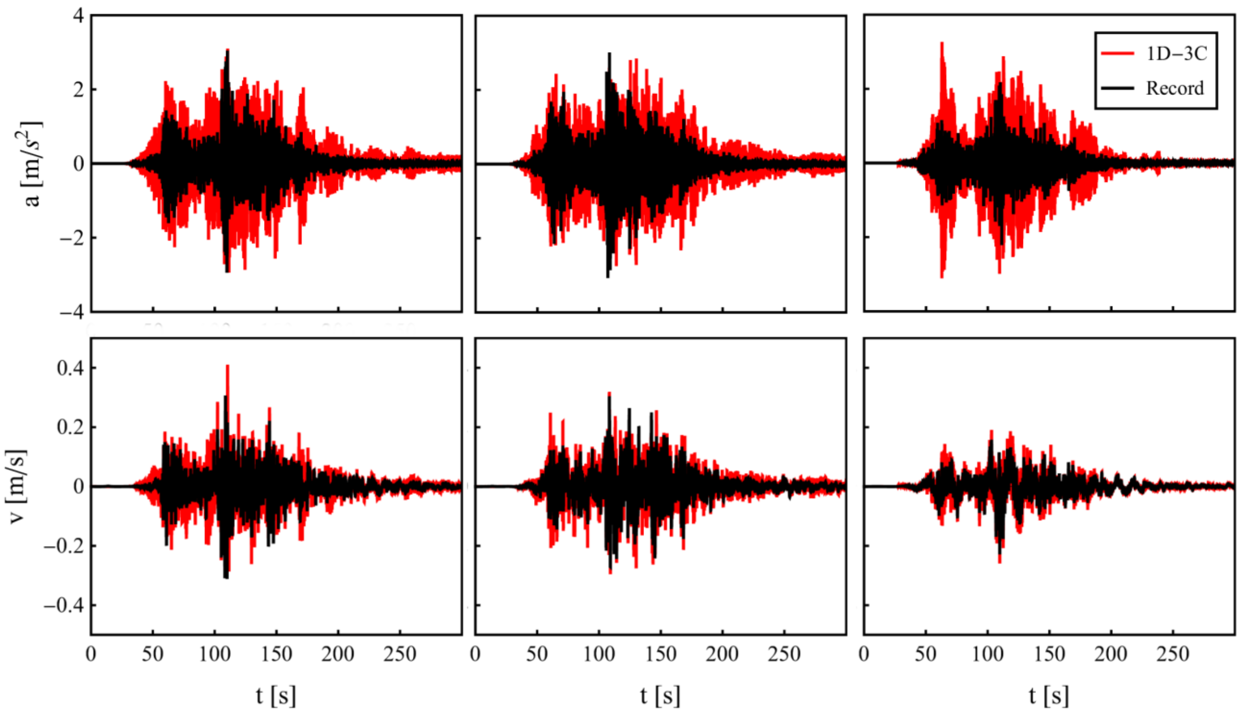

Figure 4. Time history of measured and numerical acceleration (top) and velocity (bottom), in directions NS (left), EW (middle) and UD (right), at the surface of soil profile MYGH09, during the 2011 Tohoku earthquake.

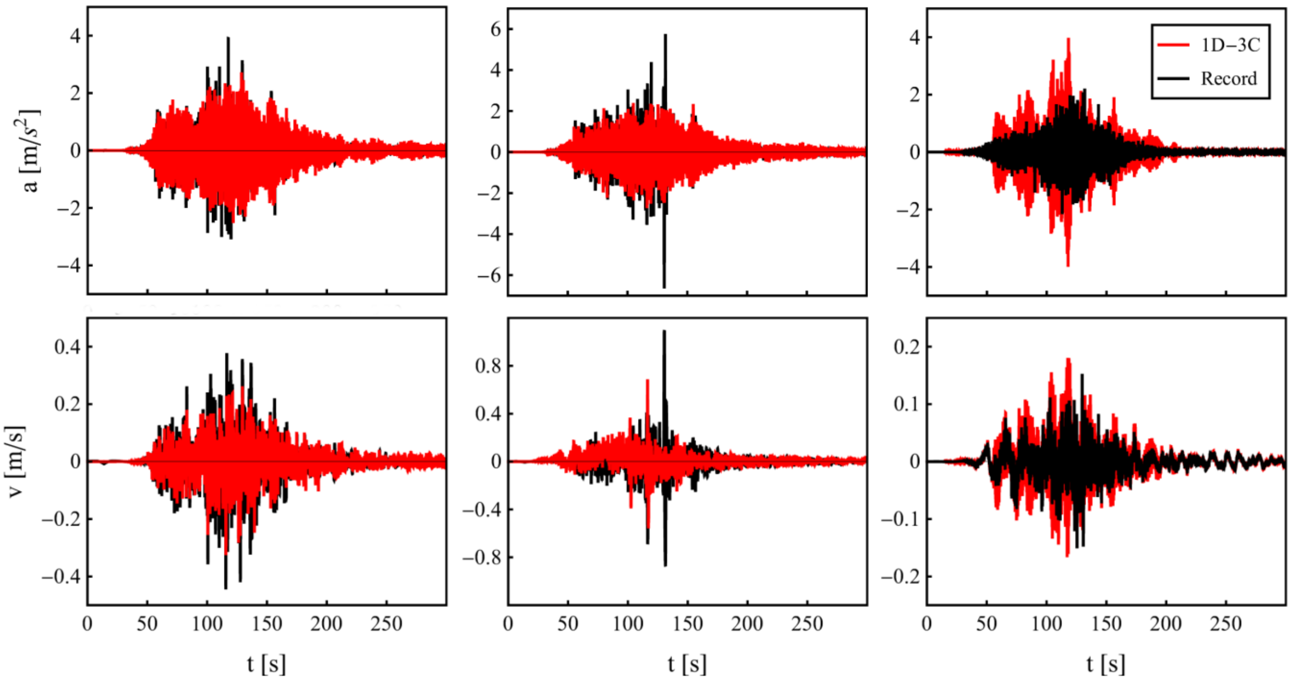

Figure 5. Time history of measured and numerical acceleration (top) and velocity (bottom), in directions NS (left), EW (middle) and UD (right), at the surface of soil profile FKSH20, during the 2011 Tohoku earthquake.

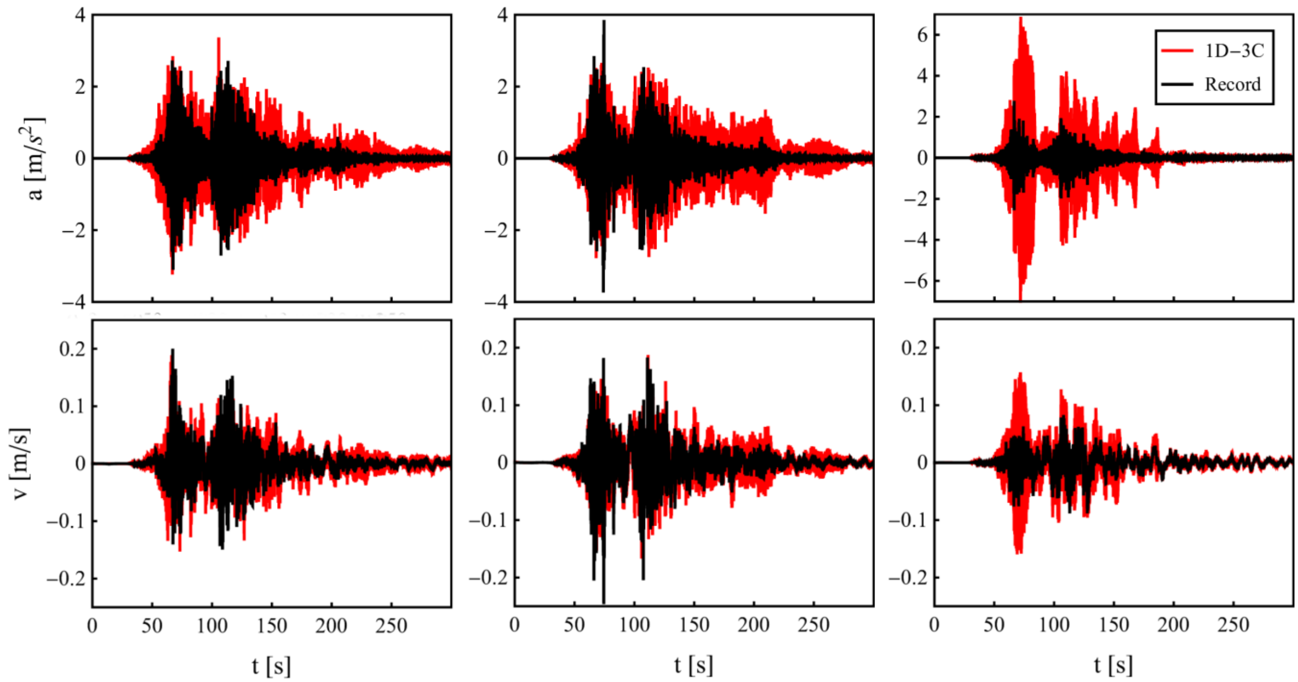

Figure 6. Time history of measured and numerical acceleration (top) and velocity (bottom), in directions NS (left), EW (middle) and UD (right), at the surface of soil profile IWTH04, during the 2011 Tohoku earthquake.

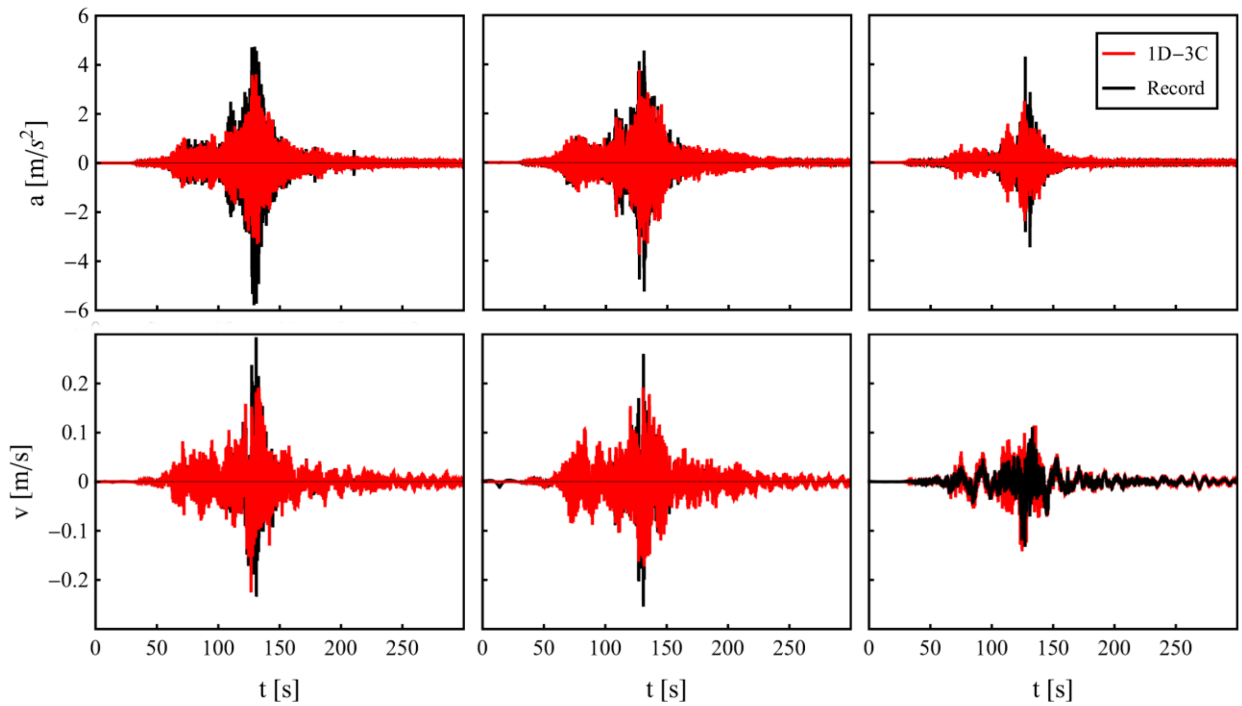

Figure 7. Time history of measured and numerical acceleration (top) and velocity (bottom), in directions NS (left), EW (middle) and UD (right), at the surface of soil profile IBRH12, during the 2011 Tohoku earthquake.

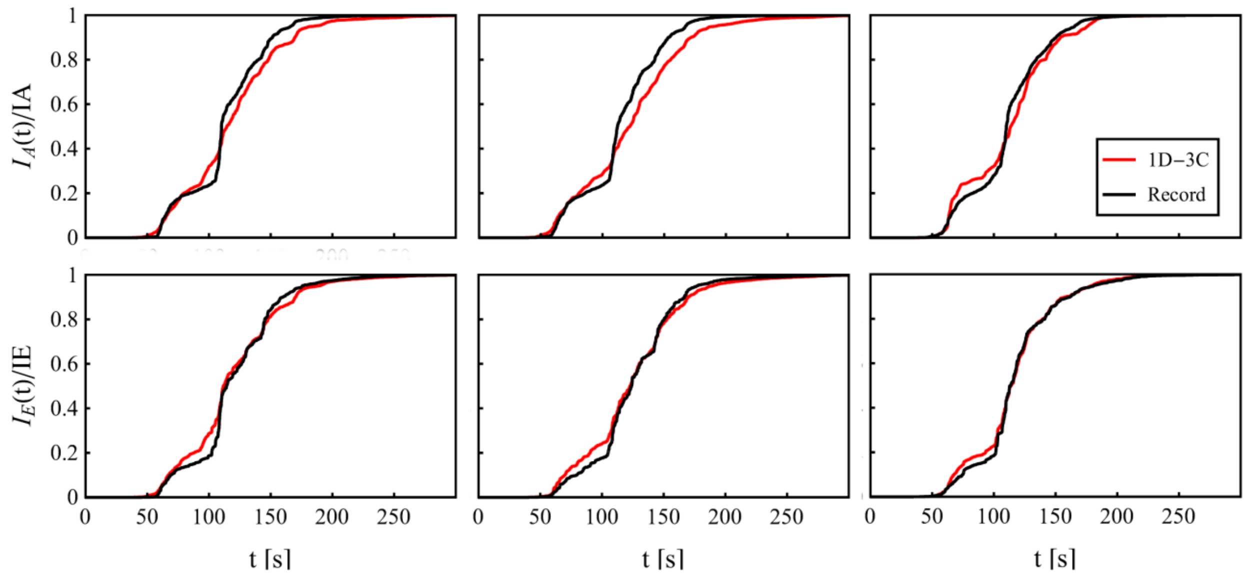

Figure 8. Normalized integral of acceleration (top) and velocity (bottom) squared for soil profile MYGH09.

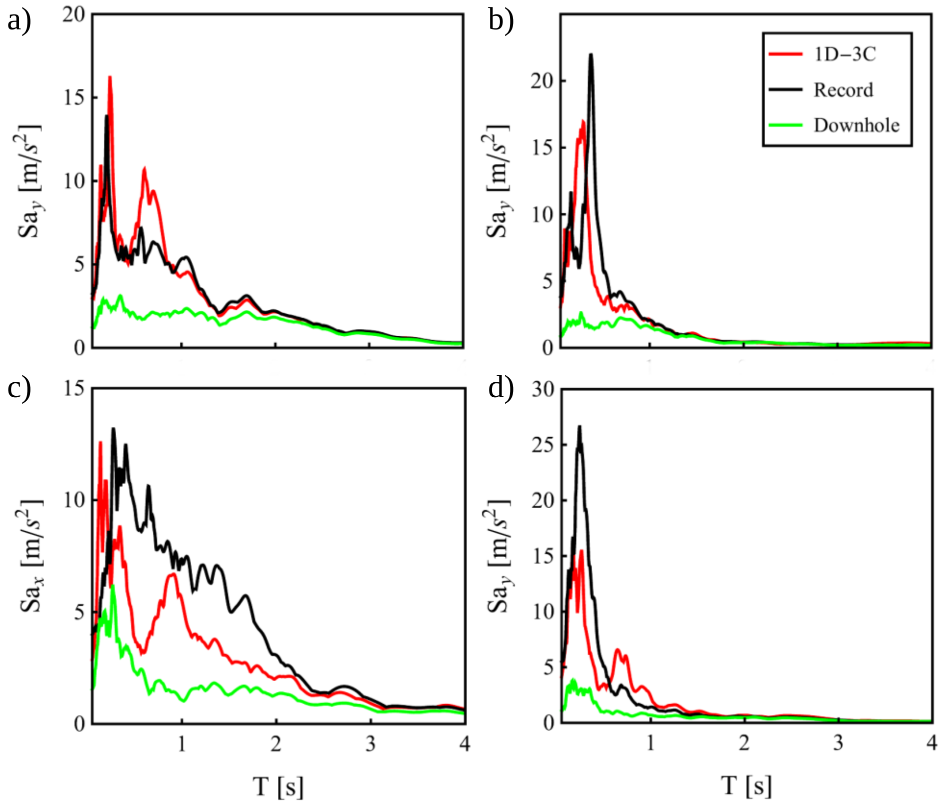

Figure 9. Numerical best fitted spectra, for soil profiles MYGH09 (a), IWTH04 (b), FKSH20 (c) and IBRH12 (d), and spectra corresponding to records at the bottom and at the surface.

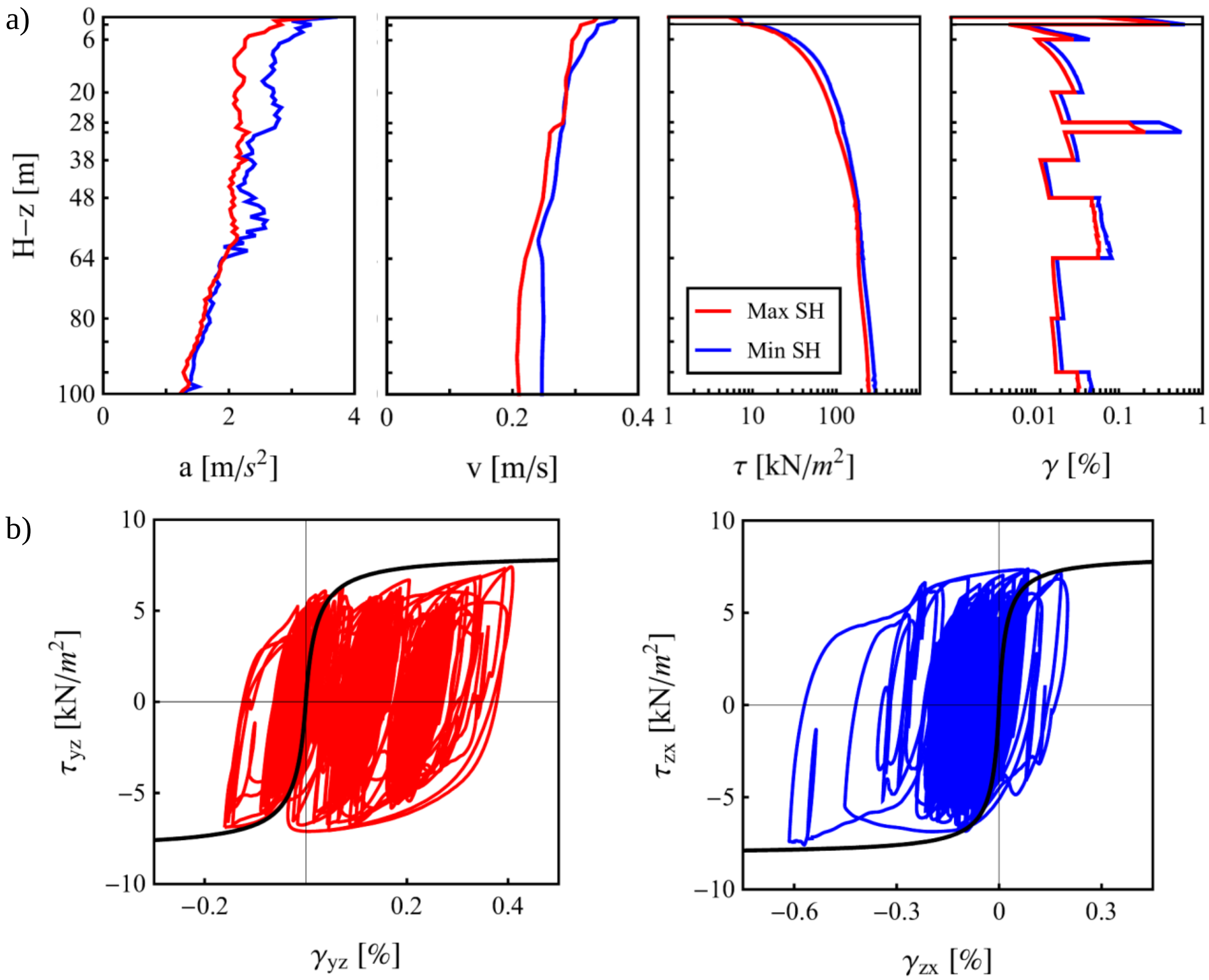

Figure 10. 1D-3C seismic response of soil profile MYGH09, during the 2011 Tohoku earthquake, in both horizontal directions of motion: acceleration, velocity, strain and stress with depth (a); shear stress-strain loops at 2 m depth (b).

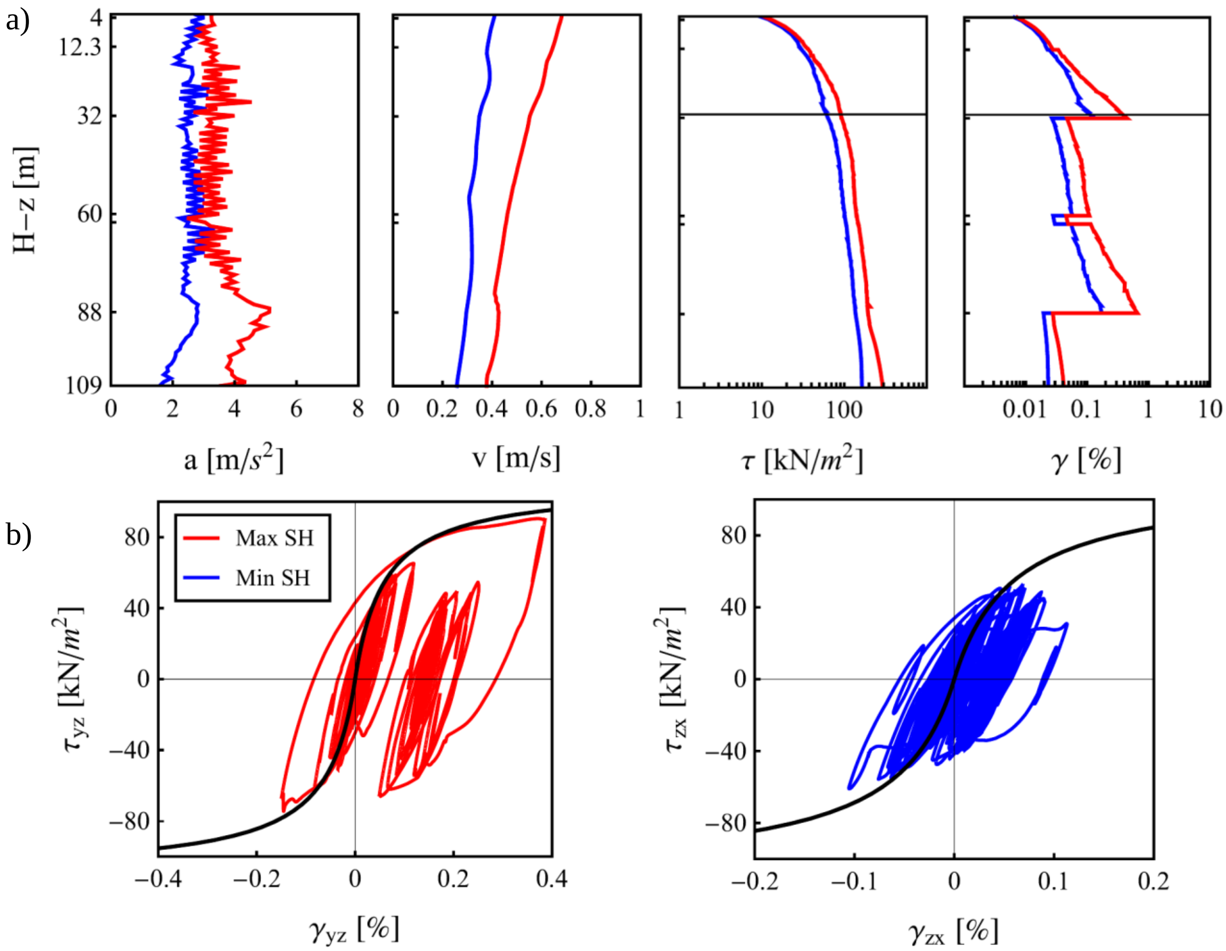

Figure 11. 1D-3C seismic response of soil profile FKSH20, during the 2011 Tohoku earthquake, in both horizontal directions of motion: acceleration, velocity, strain and stress with depth (a); shear stress-strain loops at 31 m depth (b).

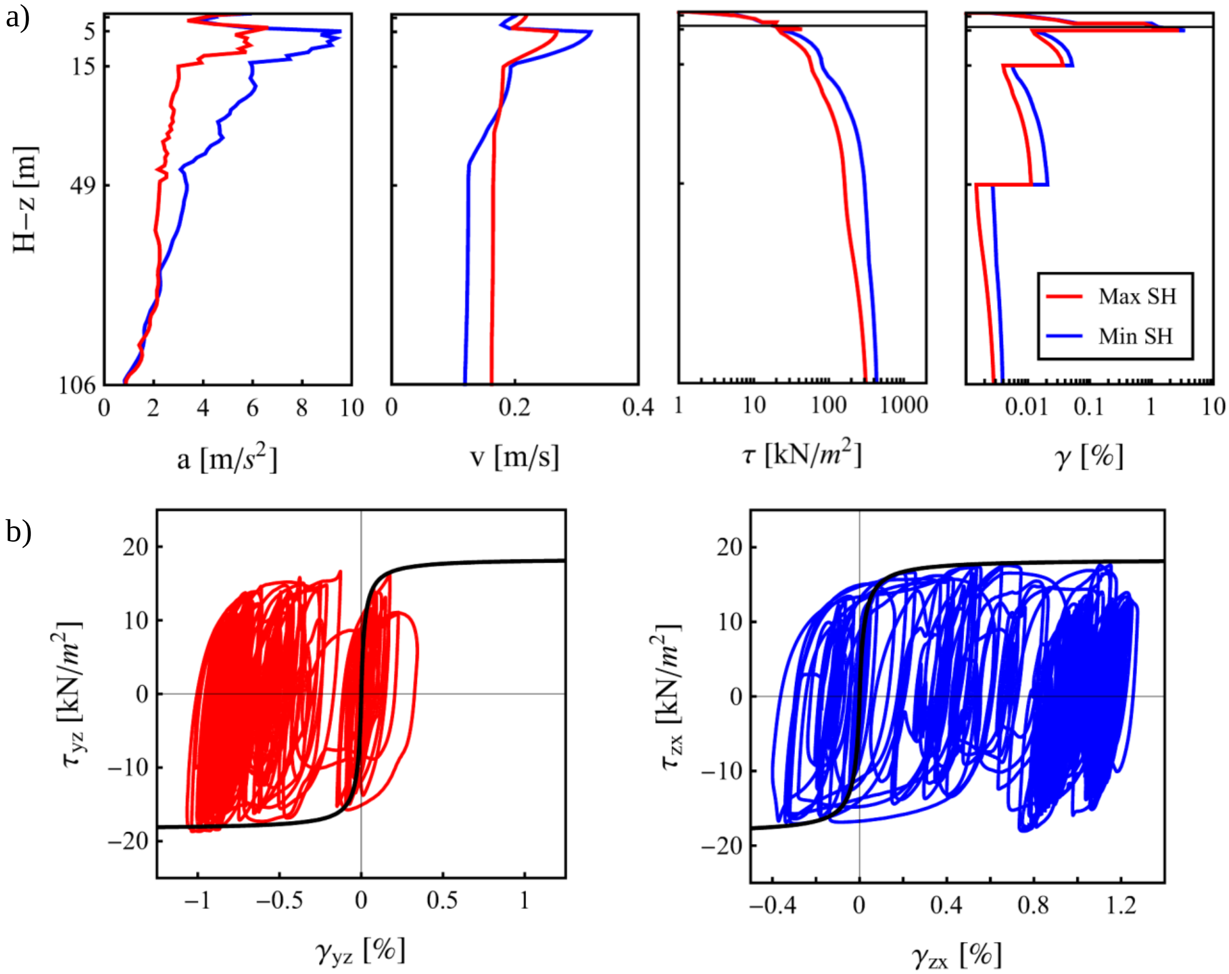

Figure 12. 1D-3C seismic response of soil profile IWTH04, during the 2011 Tohoku earthquake, in both horizontal directions of motion: acceleration, velocity, strain and stress with depth (a); shear stress-strain loops at 4 m depth (b).

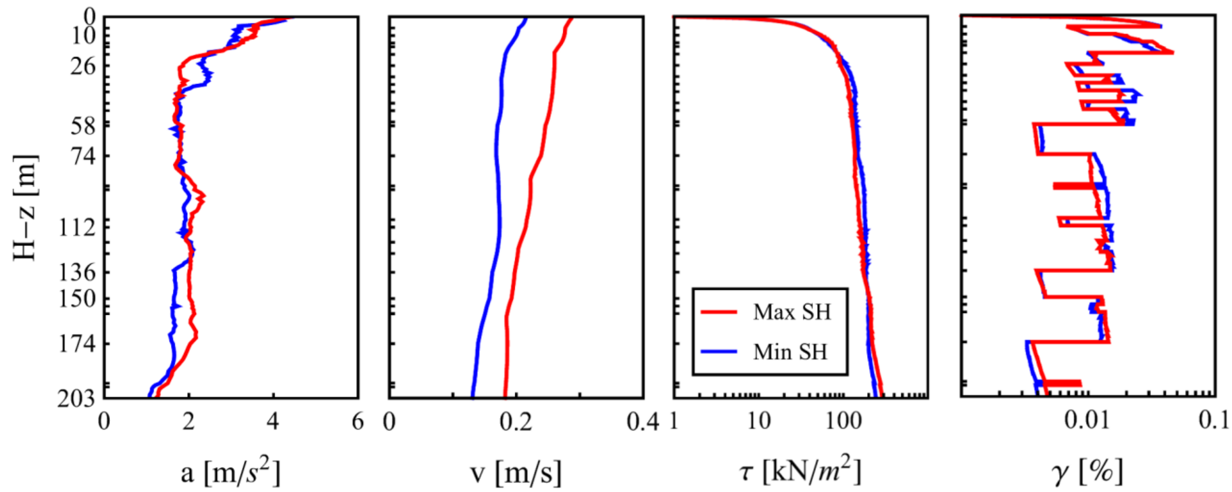

Figure 13. 1D-3C seismic response of soil profile IBRH12, during the 2011 Tohoku earthquake, in both horizontal directions of motion: acceleration, velocity, strain and stress with depth.

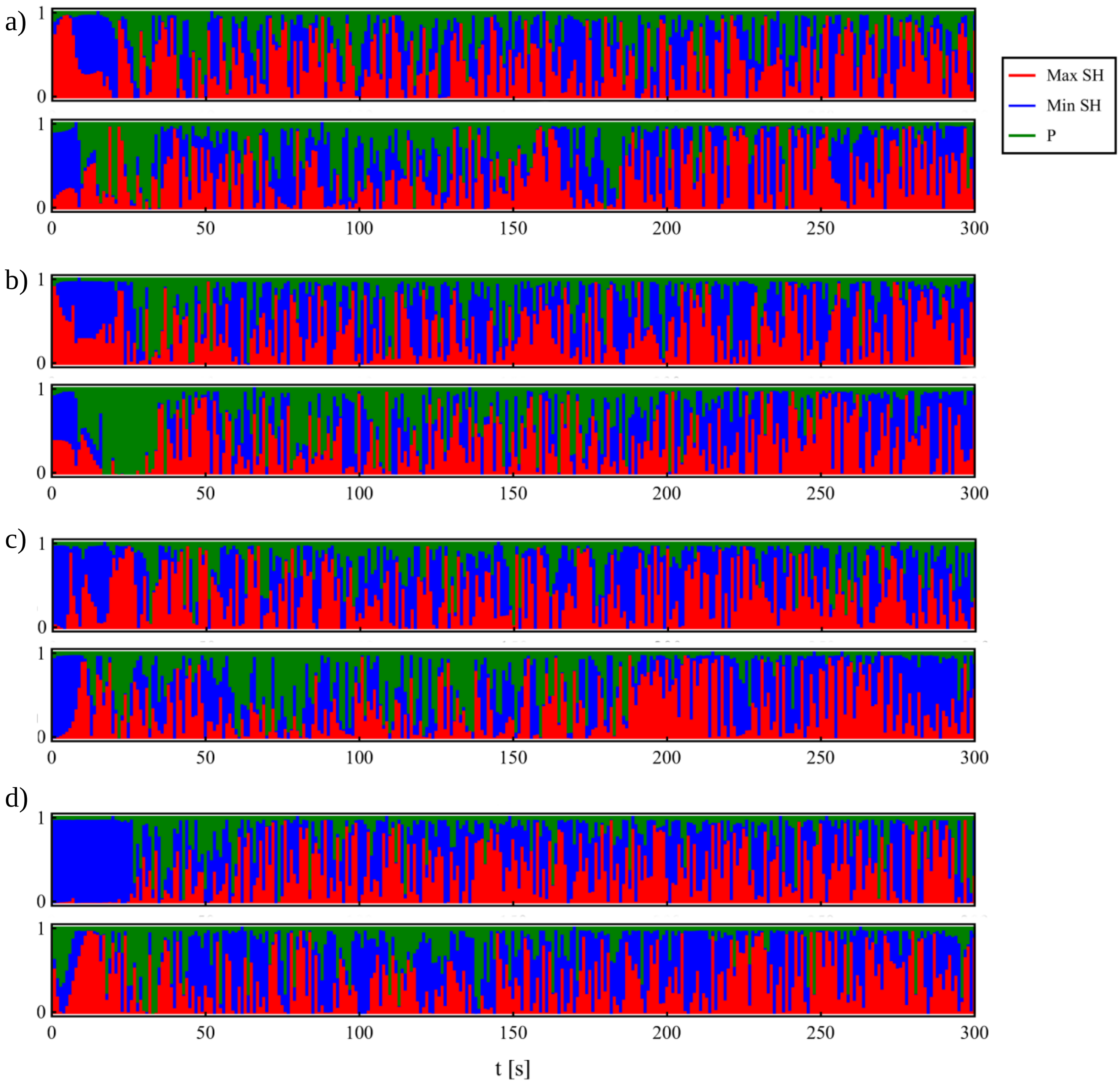

Figure 14. Recorded (top) and numerical (bottom) normalized polarization of seismic waves in terms of acceleration at the surface of soil profiles MYGH09 (a), FKSH20 (b), IWTH04 (c) and IBRH12 (d). Max SH is the PGA horizontal direction and P is the vertical direction.

APPENDIX

The assembled $(3n \times 3n)$-dimensional mass matrix $\mathbf{M}$ and the $3n$-dimensional vector of internal forces $\mathbf{F}_{\text{int}}$, in equation (2), result from the assemblage of (9×9)-dimensional matrices $\mathbf{M}^e$ and vectors $\mathbf{F}_{\text{int}}^e$, respectively, corresponding to the element e, which are expressed as

$$\mathbf{M}^e = \rho_e \int_0^{h_e} \mathbf{N}^T \, \mathbf{N} \, dz \qquad \mathbf{F}_{\text{int}}^e = \int_0^{h_e} \mathbf{B}^T \, \boldsymbol{\sigma} \, dz \tag{13}$$

where h_e is the finite element length and ρ_e is the soil density assumed constant in the element. The 6-dimensional stress and strain vectors, defined according to the hypothesis of infinite horizontal soil, are

$$\begin{aligned} \boldsymbol{\sigma} &= \begin{bmatrix} \sigma_{xx} & \sigma_{yy} & 0 & \tau_{yz} & \tau_{zx} & \sigma_{zz} \end{bmatrix}^T \\ \boldsymbol{\varepsilon} &= \begin{bmatrix} 0 & 0 & 0 & \gamma_{yz} & \gamma_{zx} & \varepsilon_{zz} \end{bmatrix}^T \end{aligned} \tag{14}$$

In equation (2), $\mathbf{N}(z)$ is the (3×9)-dimensional shape function matrix. Integrals in equation (2) are solved using the change of coordinates $z = (1+\zeta)\, h_e/2$ with $dz = h_e/2 \, d\zeta$, where $\zeta \in [-1,1]$ is the local coordinate in the element, and the Gaussian numerical integration. The shape function matrix is defined, in local coordinates, as

$$\mathbf{N}(\zeta) = \begin{bmatrix} N_1 & N_2 & N_3 & & & & & & \\ & & & N_1 & N_2 & N_3 & & & \\ & & & & & & N_1 & N_2 & N_3 \end{bmatrix} \tag{15}$$

According to Cook *et al*. (2002), $N_1 = -\zeta(1-\zeta)/2$, $N_2 = (1-\zeta^2)$ and $N_3 = \zeta(1+\zeta)/2$ are the quadratic shape functions corresponding to the three-node line element used to discretize the soil column. The terms of the (6×9)-dimensional matrix $\mathbf{B}(z)$ are the spatial derivatives of the shape functions, according to compatibility conditions and to the hypothesis of no strain variation in the horizontal directions *x* and *y*. The strain vector is defined as $\boldsymbol{\varepsilon} = \partial\, \mathbf{u}$ (Cook *et al.* 2002), where the terms of $\mathbf{u}$ are the displacements in *x*-, *y*- and *z*-direction and ∂ is a matrix of differential operators defined in such a way that compatibility equations are verified. Matrix $\mathbf{B} = \partial\, \mathbf{N}$ thus reads as follows:

$$\mathbf{B} = \begin{bmatrix} \mathbf{0}_3 & \mathbf{0}_3 & \mathbf{0}_3 & \mathbf{0}_3 & \mathbf{B}_z & \mathbf{0}_3 \\ \mathbf{0}_3 & \mathbf{0}_3 & \mathbf{0}_3 & \mathbf{B}_z & \mathbf{0}_3 & \mathbf{0}_3 \\ \mathbf{0}_3 & \mathbf{0}_3 & \mathbf{0}_3 & \mathbf{0}_3 & \mathbf{0}_3 & \mathbf{B}_z \end{bmatrix}^T \tag{16}$$

where $\mathbf{0}_3$ is a 3-dimensional null vector and $\mathbf{B}_z = \left[\partial N_1/\partial z \quad \partial N_2/\partial z \quad \partial N_3/\partial z\right]^T$ with $\partial N_i/\partial z = \left(\partial N_i/\partial \zeta\right)\left(\partial \zeta/\partial z\right)$ for $i = 1, 2, 3$ and $\partial \zeta/\partial z = 2/h_e$.

The $\left(3n \times 3n\right)$-dimensional stiffness matrix $\mathbf{K}_k^i$, in equation (3), is obtained by assembling $\left(9 \times 9\right)$-dimensional matrices as follows, with respect to element e :

$$k_k^{e,i} = \int_0^{h_e} \mathbf{B}^T\, \mathbf{E}_k^i\, \mathbf{B}\, dz \tag{17}$$

The $\left(6 \times 6\right)$-dimensional tangent constitutive matrix $\mathbf{E}_k^i$ is evaluated by the incremental constitutive relationship given by

$$\Delta \boldsymbol{\sigma}_k^i = \mathbf{E}_k^i\, \Delta \boldsymbol{\varepsilon}_k^i \tag{18}$$

According to Joyner (1975), the actual strain level and the strain and stress values at the previous time step allow to evaluate the tangent constitutive matrix $\mathbf{E}_k^i$ and the stress increment $\Delta \boldsymbol{\sigma}_k^i = \Delta \boldsymbol{\sigma}_k^i \left(\boldsymbol{\varepsilon}_k^i, \boldsymbol{\varepsilon}_{k-1}, \boldsymbol{\sigma}_{k-1}\right)$.